Microwave Down-Conversion with an Impedance-Matched # System in Driven Circuit QED

Microwave Down-Conversion with an Impedance-Matched Λ System in Driven Circuit QED

K. Inomata,[1,*] K. Koshino,[2] Z. R. Lin,[1] W. D. Oliver,[3] J. S. Tsai,[1,4] Y. Nakamura,[1,5] and T. Yamamoto[1,4,†]

[1]*RIKEN Center for Emergent Matter Science (CEMS), Wako, Saitama 351-0198, Japan*

[2]*College of Liberal Arts and Sciences, Tokyo Medical and Dental University, Ichikawa, Chiba 272-0827, Japan*

[3]*MIT Lincoln Laboratory, 244 Wood Street, Lexington, Massachusetts 02420, USA*

[4]*NEC Smart Energy Research Laboratories, Tsukuba, Ibaraki 305-8501, Japan*

[5]*Research Center for Advanced Science and Technology (RCAST), The University of Tokyo, Meguro-ku, Tokyo 153-8904, Japan*

(Received 30 April 2014; published 8 August 2014)

By driving a dispersively coupled qubit-resonator system, we realize an "impedance-matched" Λ system that has two identical radiative decay rates from the top level and interacts with a semi-infinite waveguide. It has been predicted that a photon input from the waveguide deterministically induces a Raman transition in the system and switches its electronic state. We confirm this through microwave response to a continuous probe field, observing near-perfect (99.7%) extinction of the reflection and highly efficient (74%) frequency down-conversion. These proof-of-principle results lead to deterministic quantum gates between material qubits and microwave photons and open the possibility for scalable quantum networks interconnected with waveguide photons.

DOI: 10.1103/PhysRevLett.113.063604 PACS numbers: 42.50.Pq, 03.67.Lx, 85.25.Cp

In one-dimensional optical systems, interference between an incident photon field and radiation from a quantum emitter (natural or artificial atom) is drastically enhanced due to the low dimensionality [1,2]. This may be contrasted with the three-dimensional case, where the spatial mode mismatch between the incident and scattered fields prevents perfect interference [3]. In particular, when the quantum emitter is coupled to the end of a semi-infinite waveguide and when its excited state has two radiative decay paths (i.e., a so-called Λ or Δ-type three-level system) with equal decay rates, a resonant incident photon into the emitter deterministically induces a Raman transition, and is never reflected due to destructive interference with the reemitted photon [4]. This phenomenon is called "impedance matching," in analogy with the suppression of wave reflection in an electric circuit terminated by its characteristic impedance [5].

Artificial atoms in superconducting circuits have proven to be versatile quantum mechanical systems for realizing a variety of intriguing quantum optical phenomena. In circuit quantum electrodynamics (QED) [6,7], strong coupling of a superconducting qubit with a resonator photon is readily achieved. Moreover, an artificial atom coupled directly with a microwave transmission line demonstrates near-perfect reflection of the incident field [8,9]. Recently, we have theoretically shown that an impedance-matched Λ system can be implemented by using the dressed states of a driven circuit-QED system [10]. Although Λ and Δ systems have been proposed theoretically [11–14] and implemented experimentally with a flux qubit by using the lowest three levels of its asymmetric double-well potential [15–17], realizing an impedance-matched Λ system has remained elusive. Here, we experimentally demonstrate impedance matching in the driven circuit-QED system. Using this system, we demonstrate near-perfect absorption of the incident microwave and its frequency down-conversion with a conversion efficiency of 74%. These results and their associated agreement with our model calculations indicate that each incident microwave photon deterministically induces a Raman transition in the Λ system and excites the qubit. Compared to the recently demonstrated high-efficiency capturing of an itinerant microwave pulse [18], the present scheme does not require any precise pulse shaping of the input photons, nor the time-dependent control of system parameters such as the transition energies of the artificial atom or its coupling to the waveguide. The down-conversion process is also accompanied by a flip of the qubit state, enabling its applications to quantum logic gates and memories [19] and single-photon detectors in the microwave domain [20]. This discriminates the present scheme from other frequency conversion circuits such as in Ref. [21].

We consider a flux qubit coupled to a coplanar waveguide (CPW) resonator (Fig. 1). In this coupled system, a dispersive frequency shift is enhanced by the effect of the straddling regime [22] and capacitive coupling [23,24]. Below, we treat the qubit as a two-level system since the higher energy levels of the qubit have little effect except for the enhanced dispersive shifts. The level structure of the coupled system is depicted by the Jaynes-Cummings ladder in Fig. 2(a). In the present study, only the lowest four levels are relevant because of the weak probe field applied to the resonator. We apply a drive field (frequency ω_d and power P_d) to the qubit to generate the qubit-resonator dressed

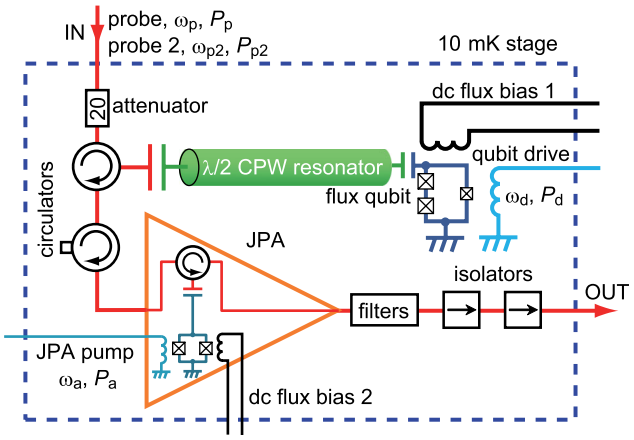

FIG. 1 (color online). Experimental setup at the 10 mK stage of a dilution refrigerator. The resonator-qubit chip and the JPA chip are mounted in separate sample packages with independent coils for dc flux bias.

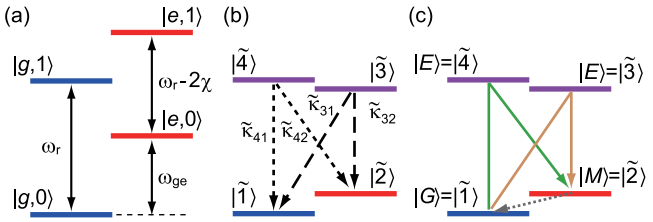

FIG. 2 (color online). Energy-level diagram of the coupled system. (a) Lowest four energy levels of the qubit-resonator coupled system. $|k,l\rangle$ denotes the eigenstates of the Jaynes-Cummings Hamiltonian, which are close to the product states $|k\rangle_q|l\rangle_r$ of the qubit and the resonator, where $k = g, e$ and $l = 0, 1, \cdots$. (b) Dressed-state energy levels in the frame rotating at ω_d. $|\tilde{i}\rangle$ represents the dressed state of the qubit-resonator coupled system, and $\tilde{\kappa}_{ij}$ is the radiative decay rate for the $|\tilde{i}\rangle \to |\tilde{j}\rangle$ transition. The nesting regime is realized when $\omega_{ge} - 2\chi < \omega_d < \omega_{ge}$. The impedance matching occurs when $\tilde{\kappa}_{41} = \tilde{\kappa}_{42}$ or $\tilde{\kappa}_{31} = \tilde{\kappa}_{32}$. (c) Raman processes in the impedance-matched Λ system (solid arrows). The $|\tilde{2}\rangle \to |\tilde{1}\rangle$ decay (dotted line) is mainly caused by qubit relaxation.

states and a probe field (frequency ω_p and power P_p) to the CPW resonator to observe their microwave response. By switching to a frame rotating at ω_d, the eigenenergies are given as

$$\omega_{|g,n\rangle} = n(\omega_r - \omega_d), \tag{1}$$

$$\omega_{|e,n\rangle} = \omega_{ge} - \omega_d + n(\omega_r - \omega_d - 2\chi), \tag{2}$$

where ω_r, ω_{ge}, and χ are the resonant frequency of the CPW resonator, the transition frequency of the qubit from the ground state $|g\rangle$ to the first excited state $|e\rangle$, and the dispersive frequency shift, respectively. Note that ω_r and ω_{ge} are not their bare frequencies but the renormalized ones including the dispersive shifts [25]. By choosing ω_d within the range of $\omega_{ge} - 2\chi < \omega_d < \omega_{ge}$, the system can be set into the "nesting regime," where the level structure becomes nested, i.e., $\omega_{|g,0\rangle} < \omega_{|e,0\rangle} < \omega_{|e,1\rangle} < \omega_{|g,1\rangle}$ [10]. The qubit drive mixes the lower (higher) two levels in Fig. 2(b) with each other to form dressed states $|\tilde{1}\rangle$ and $|\tilde{2}\rangle$ ($|\tilde{3}\rangle$ and $|\tilde{4}\rangle$). Under a proper choice of the drive power, the two radiative decay rates from $|\tilde{3}\rangle$ or $|\tilde{4}\rangle$ become identical (either $\tilde{\kappa}_{31} = \tilde{\kappa}_{32}$ or $\tilde{\kappa}_{41} = \tilde{\kappa}_{42}$). Then the coupled system functions as an impedance-matched Λ system, where the ground state $|G\rangle = |\tilde{1}\rangle$, the middle state $|M\rangle = |\tilde{2}\rangle$, and the excited state $|E\rangle = |\tilde{3}\rangle$ or, alternatively, $|\tilde{4}\rangle$ [see Fig. 2(c)]. For such a configuration, quantum interference ensures that incident photons resonant with the $|G\rangle \to |E\rangle$ transition will deterministically induce a Raman transition of $|G\rangle \to |E\rangle \to |M\rangle$. This can be observed in microwave spectroscopy as perfect absorption of the incident field and frequency down-conversion of the reflected field [10].

A schematic of the measurement setup at the 10 mK stage of a dilution refrigerator is shown in Fig. 1. The setup includes two circuits fabricated on separate chips: a flux qubit capacitively coupled to a half-wavelength CPW resonator and a flux-driven Josephson parametric amplifier (JPA). They are separately mounted in microwave-tight packages equipped with an independent coil for the flux bias and connected with each other via three circulators in series [31]. The qubit chip is the same as the one used in Ref. [23]. The qubit is biased with a half flux quantum where $\omega_{ge}/2\pi = 5.461$ GHz is insensitive to low frequency flux noise to first order. The resonator frequency $\omega_r/2\pi$ is 10.678 GHz when the qubit is in the $|g\rangle$ state. It is shifted by $-2\chi/2\pi = -80$ MHz when the qubit is in the $|e\rangle$ state.

The JPA consists of a $\lambda/4$ CPW resonator terminated by a SQUID, whose design and fabrication process are reported in Ref. [32]. The JPA is used to amplify the down-converted microwave field from the impedance-matched Λ system. Except during this particular measurement, the JPA is kept off. Namely, the amplifier pump field is turned off and the resonant frequency of its resonator is detuned from ω_r so that the JPA acts as a perfect mirror.

We first measure the reflection coefficient r of the qubit-resonator coupled system as a function of ω_p and P_d using a vector network analyzer (VNA) [Fig. 3(a)]. Microwave power levels stated in this Letter are referred to the corresponding ports on the sample chip [25]. The probe field with $P_p = -146.2$ dBm, corresponding to an average photon number of 0.013 in the resonator, is generated by the VNA, while the qubit drive field is applied from another microwave source. The qubit is continuously driven at ω_d detuned from ω_{ge} by $\delta\omega_d \equiv \omega_d - \omega_{ge} = 2\pi \times (-64)$ MHz ($|\delta\omega_d| < 2\chi$), so that the system is in the nesting regime.

For a weak drive ($P_d < -90$ dBm), the probe field is fully reflected. In contrast, as we increase P_d to $P_{d4} \equiv -84$ dBm or $P_{d3} \equiv -77$ dBm, the reflected probe field vanishes at certain frequencies. Figure 3(b) shows a

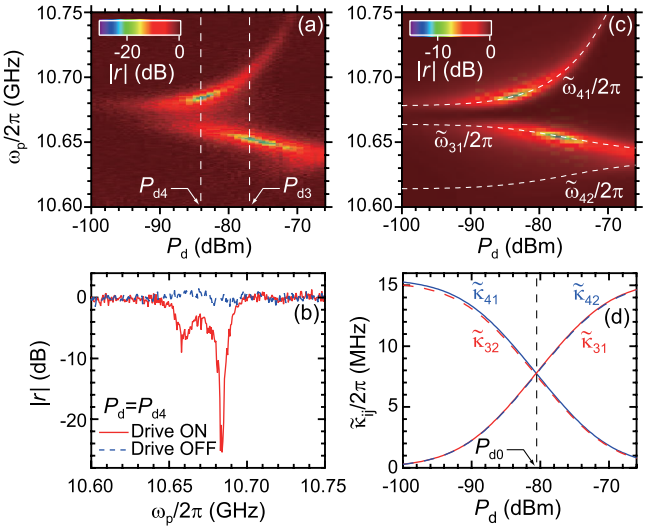

FIG. 3 (color online). Perfect absorption of the probe field. (a) Reflection coefficient $|r|$ as a function of the probe frequency ω_p and the qubit drive power P_d. The probe power is fixed at -146.2 dBm, and the detuning $\delta\omega_d$ ($\equiv\omega_d-\omega_{ge}$) is fixed at $2\pi\times(-64)$ MHz. The dashed lines show the drive powers (P_{d3} and P_{d4}) where the depth of the dips is maximized. (b) $|r|$ as a function of ω_p for $P_d=P_{d4}$. The red solid and blue dashed lines depict the data with the qubit drive on and off, respectively. (c) Numerical simulations corresponding to (a). The dashed lines indicate transition frequencies between the dressed states. (d) Calculated radiative decay rates $\tilde{\kappa}_{ij}$ as a function of P_d. The dashed line shows the drive power P_{d0}, where $\tilde{\kappa}_{41}=\tilde{\kappa}_{42}$ and $\tilde{\kappa}_{31}=\tilde{\kappa}_{32}$.

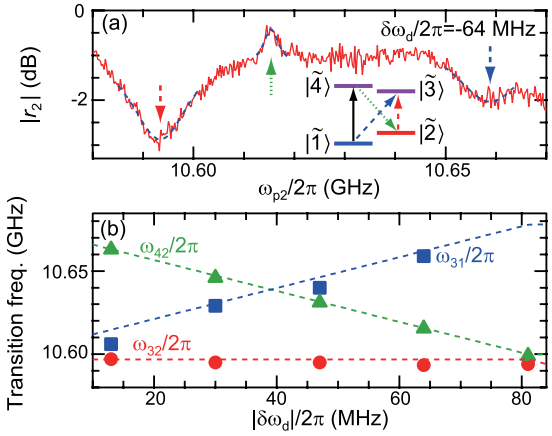

FIG. 4 (color online). Tunability of the Λ system. (a) Reflection coefficient $|r_2|$ of probe 2 as a function of ω_{p2}. Here, $\omega_p/2\pi=10.681$ GHz, $P_p=-141.2$ dBm, $P_{p2}=-135$ dBm, and $\delta\omega_d/2\pi=-64$ MHz. The dashed curves are fits with Lorentzian functions and the arrows represent center frequencies of the peak and dips. They indicate the transitions depicted in the energy-level diagram in the inset by corresponding arrows. Vertical black arrow in the inset represents the transition induced by probe 1. (b) Center frequencies of the observed peaks and dips as a function of $\delta\omega_d$. The solid symbols and dashed curves represent the measured and calculated transition frequencies, respectively.

cross section of Fig. 3(a) at P_{d4}, presenting a dip with -25 dB (99.7%) suppression at $\omega_p/2\pi=10.681$ GHz ($\approx\omega_r/2\pi$). For comparison, we theoretically calculate r and the radiative decay rates $\tilde{\kappa}_{ij}$ for the $|\tilde{i}\rangle\rightarrow|\tilde{j}\rangle$ transition [Figs. 3(c) and 3(d)] [10]. Here, we use a decay rate of a resonator photon $\kappa=\kappa_1+\kappa_2=2\pi\times16.4$ MHz, where $\kappa_1=0.95\kappa$ and $\kappa_2=0.05\kappa$ are radiative and nonradiative components, respectively, and the qubit energy decay rate $T_1^{-1}=2\pi\times0.227$ MHz, all of which are determined from independent measurements [25]. The radiative decay rate of the qubit into the drive port is set to $\gamma_c/2\pi=0.6$ kHz to adjust the horizontal scale in Fig. 3(c). We find fairly good agreement between Figs. 3(a) and 3(c). In Fig. 3(c), we draw the transition frequencies $\tilde{\omega}_{ij}$ between the state $|\tilde{j}\rangle$ and $|\tilde{i}\rangle$ by dashed curves. They indicate that the probe fields are efficiently absorbed at $(P_d,\omega_p)=(P_{d4},\tilde{\omega}_{41})$ and $(P_{d3},\tilde{\omega}_{31})$.

Figure 3(d) shows the calculated radiative decay rates from the state $|\tilde{4}\rangle$ ($\tilde{\kappa}_{41}$ and $\tilde{\kappa}_{42}$) and $|\tilde{3}\rangle$ ($\tilde{\kappa}_{31}$ and $\tilde{\kappa}_{32}$) as a function of P_d. The two radiative decay rates from each state ideally become identical at $P_d=P_{d0}\equiv-80.6$ dBm. In theory, the impedance matching is expected to occur at $(P_d,\omega_p)=(P_{d0},\tilde{\omega}_{41})$ and $(P_{d0},\tilde{\omega}_{31})$, where $\tilde{\kappa}_{41}=\tilde{\kappa}_{42}$ and $\tilde{\kappa}_{31}=\tilde{\kappa}_{32}$ [10]. In the actual system, however, inadvertent population of the $|M\rangle$ state due to the continuous probe field and the intrinsic loss of the resonator (κ_2) weaken the radiation from the Λ system, resulting in an imperfect destructive interference with the reflected wave. To compensate this effect, and thereby recover complete cancellation, the elastic component of the radiation (the $|E\rangle\rightarrow|G\rangle$ decay) should be slightly larger than the inelastic component (the $|E\rangle\rightarrow|M\rangle$ decay). As a consequence, the impedance matching occurs in practice at $(P_d,\omega_p)=(P_{d4},\tilde{\omega}_{41})$ and $(P_{d3},\tilde{\omega}_{31})$, where $\tilde{\kappa}_{41}>\tilde{\kappa}_{42}$ and $\tilde{\kappa}_{31}>\tilde{\kappa}_{32}$, respectively, as demonstrated by the pronounced dips in Figs. 3(a) and 3(c). The impedance-matched Λ systems with $|E\rangle=|\tilde{4}\rangle$ and $|E\rangle=|\tilde{3}\rangle$ [see Fig. 2(c)] are realized, correspondingly.

Next, we demonstrate that we can control the energy levels of the impedance-matched Λ system by changing $\delta\omega_d$. For this purpose, we first conduct measurements similar to Fig. 3(a) for each $\delta\omega_d$, and determine P_d for the impedance matching condition under the continuous probe field (probe 1) with a fixed P_p of -141.2 dBm and ω_p of $2\pi\times10.681$ GHz ($=\tilde{\omega}_{41}$). Then, we probe the Λ system with $|E\rangle=|\tilde{4}\rangle$ by using the VNA (probe 2) with a power $P_{p2}=-135$ dBm and frequency ω_{p2}.

Figure 4(a) shows $|r_2|$ of probe 2 as a function of ω_{p2} for $\delta\omega_d/2\pi=-64$ MHz. As indicated by arrows in Fig. 4(a), a peak and two dips are observed. The origin of these signals can be qualitatively understood by the energy-level diagram shown in the inset of Fig. 4(a). Since probe 1 continuously

drives the $|\tilde{1}\rangle \rightarrow |\tilde{4}\rangle$ transition and populates the $|\tilde{4}\rangle$ state, probe 2 stimulates the $|\tilde{4}\rangle \rightarrow |\tilde{2}\rangle$ transition when it is tuned to $\tilde{\omega}_{42}$. This is observed as the peak at $\omega_{p2}/2\pi = 10.615$ GHz, corresponding to the frequency down-conversion of probe 1. The dips at $\omega_{p2}/2\pi = 10.659$ and 10.593 GHz result from absorption of probe 2 when it is tuned to $\tilde{\omega}_{31}$ and $\tilde{\omega}_{32}$, respectively. In Fig. 4(b), we plot center frequencies of these peaks and dips for different $\delta\omega_d$'s. As expected, $\tilde{\omega}_{31}$ ($\tilde{\omega}_{42}$) is an increasing (a decreasing) function of $|\delta\omega_d|$, whereas $\tilde{\omega}_{32}$ is independent of $\delta\omega_d$. To understand this result quantitatively, we calculated the transition frequencies. They are plotted by dashed curves in Fig. 4(b), and agree well with the experimental data. Note that the impedance matching is not realized any more at $|\delta\omega_d|/2\pi = 81$ MHz in Fig. 4(b) because $|\delta\omega_d| > 2\chi$.

In the above measurement, we indirectly observed the frequency down-conversion of probe 1 as a stimulated emission peak in $|r_2|$. Now we directly measure the down-converted signal from the impedance-matched Λ system with $|E\rangle = |\tilde{4}\rangle$. In this measurement, we use a flux-driven JPA to amplify the weak signal. The JPA is operated in a nondegenerate mode at 10.6145 GHz, with a signal gain of 21 dB and a bandwidth of $2\pi \times 3.3$ MHz. The qubit is driven at $\delta\omega_d/2\pi = -64$ MHz, and a probe power P_p of -146.2 dBm is injected. To improve the signal-to-noise ratio, which is below unity even with the JPA, we repeatedly turn on and off the qubit drive [33], and average the difference in the spectral density 4×10^4 times using a spectrum analyzer.

Figure 5(a) shows the obtained down-converted spectrum. Two peaks appear symmetrically with respect to the band center of the JPA, corresponding to the signal and idler components of the JPA output. The JPA output power is given by

$$P_{\text{out}}(\omega) = [G_s(\omega)S_{\text{in}}(\omega) + G_i(\omega_a - \omega)S_{\text{in}}(\omega_a - \omega)]B, \quad (3)$$

where ω_a is the JPA pump frequency, $B = 2\pi \times 10$ kHz is the resolution bandwidth of the spectrum analyzer, and S_{in} is the power spectral density of the down-converted signal, which we assume to have a Lorentzian line shape with a center frequency of ω_s. G_s and G_i are the signal and idler gains of the JPA which are almost identical within the measurement range. By fitting the measured spectrum with Eq. (3) [solid curve in Fig. 5(a)], we extracted $S_{\text{in}}(\omega)$ as shown in Fig. 5(b), and obtained $\omega_s = 2\pi \times 10.6157$ GHz and $\delta\omega = 2\pi \times 1.210$ MHz, where $\delta\omega$ is a linewidth of the signal. The signal frequency ω_s agrees very well with the frequency of the stimulated emission peak in Fig. 4(a), while $\delta\omega$ is 6 times larger than the expected value (the $|\tilde{2}\rangle \rightarrow |\tilde{1}\rangle$ decay rate, which roughly coincides with T_1^{-1}) [34]. A possible reason for this is inhomogeneous broadening due to fluctuations of ω_{ge} during the measurement which takes nearly three hours.

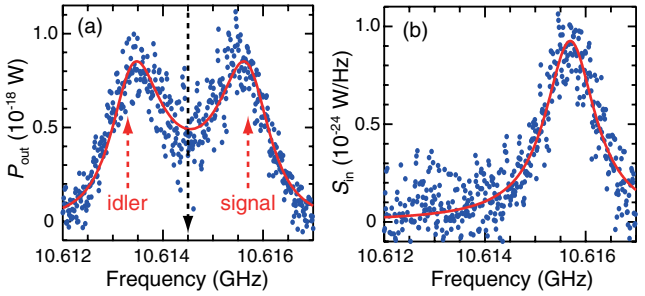

FIG. 5 (color online). Down-conversion of the microwave field. (a) Output power of the JPA. Blue dots are the measurement data and the solid line is a fit with Eq. (3). A JPA with $G_s = 21$ dB and a bandwidth of $2\pi \times 3.3$ MHz was used. The black arrow indicates the band center of the JPA. (b) Extracted power spectral density of the down-converted signal. The solid line shows calculated S_{in} with parameters obtained by the fitting in (a).

From the data in Fig. 5(b), we estimate the down-conversion efficiency η, which is defined by the flux of down-converted photons normalized by the input flux. The signal power P_s obtained by integrating the down-converted signal in Fig. 5(b) is $(1.77 \pm 0.20) \times 10^{-18}$ W, while the input probe power P_p is $10^{-17.62}$ W. From these values, $\eta(= P_s\omega_p/P_p\omega_s)$ is determined to be $74 \pm 8\%$, where the uncertainty comes from the inaccuracy in the estimation of the total gain (± 0.5 dB) in the output microwave lines. On the other hand, a theoretical estimation based on the experimental parameters gives η of 68% [25]. The reduction of η from unity is attributed to the intrinsic loss of the resonator and the incomplete initialization of the ground state $|\tilde{1}\rangle$ due to continuous excitation by the probe. Although it is difficult to confirm in the present setup due to an insufficient signal-to-noise ratio, we expect, for a weaker continuous wave or single microwave photons as the probe, nearly complete down-conversion of $\eta \simeq 95\%$ $(= \kappa_1/\kappa)$.

In conclusion, we experimentally realized an impedance-matched Λ system using dressed-state engineering of a driven circuit-QED system, here a superconducting flux qubit and CPW resonator connected to a semi-infinite transmission line. The results lead to deterministic quantum gates between material qubits and microwave photons and open the possibility for scalable quantum networks interconnected with waveguide photons.

We would like to thank O. Astafiev for technical help, and V. Bolkhovsky and G. Fitch for assistance with the JPA fabrication at MIT-LL. Sputtered Nb films were fabricated in the clean room for analogue-digital superconductivity (CRAVITY) in the National Institute of Advanced Industrial Science and Technology (AIST). This work was supported by the Funding Program for World-Leading Innovative R&D on Science and

Technology (FIRST), the Grant-in-Aid for Scientific Research Program for Quantum Cybernetics of the Ministry of Education, Culture, Sports, Science, and Technology (MEXT), Japan, and the NICT Commissioned Research.

*kunihiro.inomata@riken.jp
†t-yamamoto@fe.jp.nec.com

[1] M. J. Collett and C. W. Gardiner, Phys. Rev. A **30**, 1386 (1984).
[2] J.-T. Shen and S. Fan, Opt. Lett. **30**, 2001 (2005).
[3] G. Zumofen, N. M. Mojarad, V. Sandoghdar, and M. Agio, Phys. Rev. Lett. **101**, 180404 (2008).
[4] K. Koshino, Phys. Rev. A **79**, 013804 (2009).
[5] M. Afzelius and C. Simon, Phys. Rev. A **82**, 022310 (2010).
[6] A. Blais, R.-S. Huang, A. Wallraff, S. M. Girvin, and R. J. Schoelkopf, Phys. Rev. A **69**, 062320 (2004).
[7] A. Wallraff, D. I. Schuster, A. Blais, L. Frunzio, R.-S. Huang, J. Majer, S. Kumer, S. M. Girvin, and R. J. Schoelkopf, Nature (London) **431**, 162 (2004).
[8] O. Astafiev, A. M. Zagoskin, A. A. Abdumalikov, Jr., Y. A. Pashkin, T. Yamamoto, K. Inomata, Y. Nakamura, and J. S. Tsai, Science **327**, 840 (2010).
[9] I.-C. Hoi, C. M. Wilson, G. Johansson, T. Palomaki, B. Peropadre, and P. Delsing, Phys. Rev. Lett. **107**, 073601 (2011).
[10] K. Koshino, K. Inomata, T. Yamamoto, and Y. Nakamura, Phys. Rev. Lett. **111**, 153601 (2013).
[11] Z. Zhou, Shih-I Chu, and S. Han, Phys. Rev. B **66**, 054527 (2002).
[12] Z. Kis and E. Paspalakis, Phys. Rev. B **69**, 024510 (2004).
[13] Y.-X. Liu, J. Q. You, L. F. Wei, C. P. Sun, and F. Nori, Phys. Rev. Lett. **95**, 087001 (2005).
[14] J. Siewert and T. Brandes, Adv. Solid State Phys. **44**, 181 (2004).
[15] K. V. R. M. Murali, Z. Dutton, W. D. Oliver, D. S. Crankshaw, and T. P. Orlando, Phys. Rev. Lett. **93**, 087003 (2004).
[16] M. Grajcar, S. H. W. van der Ploeg, A. Izmalkov, E. Il'ichev, H.-G. Meyer, A. Fedorov, A. Shnirman, and G. Schön, Nat. Phys. **4**, 612 (2008).
[17] S. O. Valenzuela, W. D. Oliver, D. M. Berns, K. K. Berggren, L. S. Levitov, and T. P. Orlando, Science **314**, 1589 (2006).
[18] J. Wenner, Y. Yin, Y. Chen, R. Barends, B. Chiaro, E. Jeffrey, J. Kelly, A. Megrant, J. Y. Mutus, C. Neill, P. J. J. O'Malley, P. Roushan, D. Sank, A. Vainsencher, T. C. White, A. N. Korotkov, A. N. Cleland, and J. M. Martinis, Phys. Rev. Lett. **112**, 210501 (2014).
[19] K. Koshino, S. Ishizaka, and Y. Nakamura, Phys. Rev. A **82**, 010301(R) (2010).
[20] Y.-F. Chen, D. Hover, S. Sendelbach, L. Maurer, S. T. Merkel, E. J. Pritchett, F. K. Wilhelm, and R. McDermott, Phys. Rev. Lett. **107**, 217401 (2011).
[21] B. Abdo, K. Sliwa, F. Schackert, N. Bergeal, M. Hatridge, L. Frunzio, A. D. Stone, and M. Devoret, Phys. Rev. Lett. **110**, 173902 (2013).
[22] J. Koch, T. M. Yu, J. Gambetta, A. A. Houck, D. I. Schuster, J. Majer, A. Blais, M. H. Devoret, S. M. Girvin, and R. J. Schoelkopf, Phys. Rev. A **76**, 042319 (2007).
[23] K. Inomata, T. Yamamoto, P.-M. Billangeon, Y. Nakamura, and J. S. Tsai, Phys. Rev. B **86**, 140508(R) (2012).
[24] T. Yamamoto, K. Inomata, K. Koshino, P.-M. Billangeon, Y. Nakamura, and J. S. Tsai, New J. Phys. **16**, 015017 (2014).
[25] See Supplemental Material at http://link.aps.org/supplemental/10.1103/PhysRevLett.113.063604 for details on the calibration of the probe power and the numerical calculations, which includes Refs. [26–30].
[26] I. Siddiqi, R. Vijay, F. Pierre, C. M. Wilson, M. Metcalfe, C. Rigetti, L. Frunzio, and M. H. Devoret, Phys. Rev. Lett. **93**, 207002 (2004).
[27] M. Watanabe, K. Inomata, T. Yamamoto, and J.-S. Tsai, Phys. Rev. B **80**, 174502 (2009).
[28] D. M. Pozer, *Microwave Engineering* (Addison-Wesley, Reading, MA, 1990).
[29] C. P. Wen, IEEE Trans. Microwave Theory Tech. **17**, 1087 (1969).
[30] K. Inomata, T. Yamamoto, M. Watanabe, K. Matsuba, and J.-S. Tsai, J. Vac. Sci. Technol. B **27**, 2286 (2009).
[31] Z. R. Lin, K. Inomata, W. D. Oliver, K. Koshino, Y. Nakamura, J. S. Tsai, and T. Yamamoto, Appl. Phys. Lett. **103**, 132602 (2013).
[32] T. Yamamoto, K. Inomata, M. Watanabe, K. Matsuba, T. Miyazaki, W. D. Oliver, Y. Nakamura, and J. S. Tsai, Appl. Phys. Lett. **93**, 042510 (2008).
[33] The measurement with the qubit drive off calibrates the JPA gain. To compensate fluctuations of the JPA gain, we determine the gain in every measurement.
[34] K. Koshino, K. Inomata, T. Yamamoto, and Y. Nakamura, New J. Phys. **15**, 115010 (2013).